Photoelectron spectroscopy and electronic structure of heavy group IV–VI diatomics

Lai-Sheng Wang, B. Niu, Y. T. Lee, and D. A. Shirley
Department of Chemistry, University of California and Materials and Chemical Sciences Division, Lawrence Berkeley Laboratory, 1 Cyclotron Road, Berkeley, California 94720

K. Balasubramanian[a)]
Department of Chemistry, Arizona State University, Tempe, Arizona 85287-1604

(Received 12 September 1989; accepted 11 October 1989)

Vibrationally resolved HeI (584 Å) photoelectron spectra of the heavy group IV–VI diatomics SnSe, SnTe, PbSe, and PbTe were obtained with a new high temperature molecular beam source. Ionization potentials and spectroscopic constants are reported for all the ionic states observed. Relativistic complete active space multiconfiguration self-consistent field (MCSCF) followed by multireference singles + doubles relativistic configuration interaction (CI) calculations which included up to 200 000 configurations were made on both the neutral diatomics and their positive ions. Ionization potentials and spectroscopic constants were calculated and were in good agreement with the experimentally measured values. Relativistic CI potential energy curves were calculated for all the neutral ground states and the ionic states involved. Relativistic effects were shown to play an important role in these heavy diatomics. The $^2\Sigma^+_{1/2}$ and $^2\Pi_{1/2}$ states for all four molecular ions showed avoided curve crossings, which resulted in pronounced shoulders in the $\Omega = 1/2$ potential energy curves of $PbTe^+$. Experimentally, autoionization transitions were also observed for the $PbTe^+$ spectrum. The importance of the relativistic effect and chemical bonding in the heavy diatomics are discussed.

I. INTRODUCTION

The heavy group IV–VI diatomics SnSe, SnTe, PbSe, and PbTe are interesting at least in two respects. The bulk materials corresponding to these molecules are low band gap semiconductors[1] and have been the subjects of numerous investigations due to their technological importance as infrared and visible radiation detectors. Clusters of these molecules, which conceptually link the individual molecules to the bulk, may soon also become important subjects of study.[2,3] A detailed understanding of the monomers would be the first step toward the understanding of the series through cluster species up to bulk properties. On the other hand, these diatomics molecules are interesting in their own right, because relativistic effects are expected to play an important role in the chemistry of heavy elements,[4] and these molecules provide some good examples of these effects in small chemical systems.

Photoelectron spectroscopy is the method of choice because it gives unique information about the electronic properties of matter.[5] Study of the photoelectron spectra of heavy group IV–VI molecules has been hindered mainly by the difficulty of producing the molecules in the gas phase. Consequently, there have been very few reports on these molecules. In particular, there have been no studies on the lead chalcogenides except a tentative one by Wu and Fehlner.[6] They also obtained the spectra of GeS, GeSe, SnS, and SnTe, at a low signal level and resolution. White *et al.*[7] studied all the germanium and tin chalcogenides with about 85 meV resolution. A few oxides also have been studied: GeO,[8] SiO,[9] and SnO.[10]

Theoretically, there have been no studies on the molecules reported here, except for PbSe.[11–13] Theoretical investigations are available for other lighter group IV–VI diatomics: SnO,[13,14] SnS,[15] PbO,[13,16] and PbS.[11–13,17] The information accumulated to date on the spectroscopic constants and potential energy curves of heavy *p*-block elements hydrides, halides and chalcogenides have been reviewed recently by one of the authors (K.B.).[18]

In the present study, we combined experiment and theory, trying to understand the bonding and the relativistic effects in these heavy diatomics systematically. We have obtained high resolution HeI (584 Å) photoelectron spectra of SnSe, SnTe, PbSe, and PbTe, with a new high temperature molecular beam source. Vibrational structure was resolved for all the spectra except for the Π bands of $PbTe^+$, which has very low vibrational frequencies, on the order of our resolution (15–20 meV). With a Franck–Condon factor analysis, we were able to obtain all the spectroscopic constants for all the relevant ionic states. We carried out relativistic quantum chemical calculations to compare with and assist the interpretation of the experimental results.

In what follows, we will give a brief account of the experimental apparatus in Sec. II, and the theoretical method in Sec. III. The results and data analysis are presented in Sec. IV. We discuss the results in Sec. V. The conclusions are given in Sec. VI.

II. EXPERIMENTAL

The experimental apparatus has two principal parts: the photoelectron spectrometer and the high temperature molecular beam source. The former has been described in detail elsewhere.[19] It consists of a helium discharge lamp, a quadrupole mass spectrometer and a hemispherical electron ener-

[a)] Camille and Henry Dreyfus Teacher–Scholar.

 0021-9606/90/020899-10$03.00

gy analyzer with multichannel detection. The design and operating principles of the high temperature molecular beam source were documented in Ref. 20, but some important modifications have been made, which have improved the workability of the source. The detailed design, application and operating procedures will be published separately.[21] Only aspects related to the current experiments will be given here.

A schematic cross-sectional view of the oven is shown in Fig. 1. The basic idea is to employ electron bombardment heating to eliminate the stray field associated with simpler resistive heating for high resolution work. The goal is to generate an intense, continuous and entrained supersonic molecular beam suitable for our photon source (HeI discharge lamp) and the high resolution requirements. The oven consists of a 0.51 mm coiled W filament (15, Fig. 1) for thermionic emission, a Mo cylinder electrostatic deflector (9, Fig. 1), inner and outer W vacuum jackets (12 and 13, Fig. 1), a graphite crucible (11, Fig. 1) and the carrier gas inlet system (1, Fig. 1). The W filament is noninductively wound, supported by a ceramic filament support (14, Fig. 1), and screw mounted onto two Mo filament mount posts (8, Fig. 1). The bus, supplying power for the filament and running through the triple-tubing section (19, also see 17 in Fig. 2), is not shown in Fig. 1. The filament and the Mo electrostatic deflector are floated at negative high voltage with respect to the surroundings, and are insulated from the surroundings through the ceramic high voltage standoff (16, Fig. 1). Hence, the electrons emitted from the filament are accelerated toward the inner W vacuum jacket, which in turn heats up the crucible radiatively. The inner and outer W vacuum jackets define a different vacuum region which is pumped by a 200 l/s Turbo pump (see Fig. 2). This is necessary to be able to operate under high voltage conditions. The crucible is spring pressed against the inner vacuum jacket to allow the necessary thermal expansion (also see 3 and 4 in Fig. 2). The top of the crucible, which makes direct contact with the inner jacket, is therefore the hottest part of the crucible. This is essential to assure that the nozzle not be clogged.

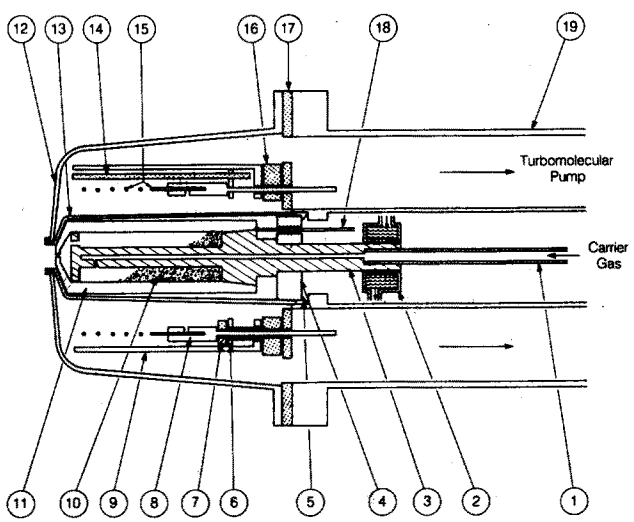

FIG. 1. A cross sectional view of the oven assembly. (1) Ta carrier gas inlet tube, (2) water cooling block, (3) graphite crucible cap, (4) graphite radiation shield, (5) Mo springy conduction barrier, (6) Mo retainer, (7) ceramic insulator, (8) Mo filament mount post, (9) Mo electrostatic deflector and radiation shield, (10) sample, (11) graphite crucible body, (12) outer W (or Ta) vacuum jacket, (13) inner W (or Ta) vacuum jacket, (14) ceramic filament support rod, (15) W filament, (16) ceramic high voltage standoff, (17) Mo (or ceramic) support plate for filament post, (18) thermocouple, (19) stainless steel triple-tubed flange section (shown in twofold symmetry for easier viewing). Not shown are the bus lines, some radiation shields, and W wires for supporting the filament.

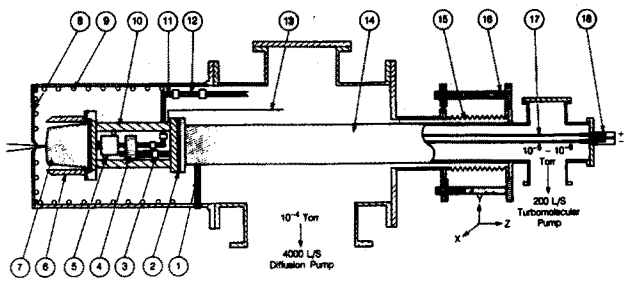

FIG. 2. Schematic view of the high temperature molecular beam source. (1) rods for fine alignment of the nozzle and skimmer (showing one of three), (2) ceramic spacer, (3) guiding rod, spring, and lock nuts for spring loading (showing one of three), (4) clamp base plate (receiving spring force), (5) water cooling block, (6) water-cooled thermal shield, (7) oven assembly (shown in Fig. 1), (8) reducer cap, (9) water cooling coil, (10) triple-tubed flange, (11) carrier gas inlet line, (12) ceramic insulating tube, (13) emission return conductor (input for filament control system), (14) stainless steel arm, (15) bellows, (16) XYZ translation stage, (17) filament busbar, (18) vacuum feedthroughs. Not shown are the various water lines and thermocouples. All water lines have electrical breaks and are made of flexible tubing or plastic tubing to free the motion of the stainless steel arm.

Figure 2 shows the overall view of the beam source. The conical skimmer, which has a diameter of 5.1 mm, is not heated. The skimmer diameter is much bigger than normal so as not to have the skimmer clogged during the course of a single experiment. The nozzle and skimmer alignment is achieved through the XYZ translation stage (15 and 16, Fig. 2) and the fine alignment rods (1, Fig. 2). The design power of the oven was 1.5 KW. We can operate the source at 1 KW safely, which would raise the crucible temperature to above 2000 K. The thermal loss at the back of the crucible often makes it difficult to evaporate very refractory materials. For the experiments reported here, less than 500 W power was needed in all cases.

The nozzle-skimmer alignment and the size of the nozzle are also important factors. A large nozzle and good alignment would facilitate lower temperature evaporations, so the heating power and temperature measurement (18, Fig. 1) only have relative meanings. In general, we need about 1 to 10 Torr of vapor pressure in order to obtain an acceptable spectrum. We normally heat up the oven slowly at the beginning for the source to outgas, using the quadrupole mass spectrometer to monitor the beam. Then we continuously raise the temperature until a reasonable photoelectron signal strength is achieved.

The SnSe, SnTe, PbSe, and PbTe diatomics are known to be stable vapor species.[22–24] We only observed minor amounts of Se_2 and Te_2 as outgases for the SnSe and SnTe runs at low temperatures.[25] All samples were purchased commercially from CERAC with better than 98% purity. The experimental conditions are listed in Table I. The temperatures were measured at the rear of the crucible (18, Fig.

TABLE I. The experimental conditions.

	SnSe	SnTe	PbSe	PbTe
T (K)[a]	990	1090	1010	1000
P (Torr)[b]	200(He)	600(Ne)	500(Ne)	600(He)
ϕ (mm)[c]	0.15	0.10	0.13	0.14
Power (mAxV)[d]	230×1050	500×750	300×1400	250×1250
Tvib (K)[e]	300 ± 50	470 ± 50	500 ± 50	350 ± 50

[a] Temperatures measured with type K (Chromel-Alumel) thermocouples at the rear of the graphite crucibles. They were only relative measures, and are about 100–200 deg lower than the effective sample temperatures.
[b] Carrier gas pressures.
[c] Nozzle diameters.
[d] Heating powers. About 60–80 Watts power was needed to drive the tungsten filaments. This power was in addition to the heating powers.
[e] Vibrational temperatures, obtained through Franck–Condon analyses. See the text.

1), and are usually 100 to 200 deg lower than the effective evaporation temperatures. The carrier gas types and pressures were not optimized for each individual experiment. For the PbTe run alone, we used both He and Ne carrier gases, which gave effectively identical spectra. We were able to estimate vibrational temperatures (Tvibs) of the molecules in the beams from hot band transitions with Franck–Condon analyses (see Sec. IV). These are also listed in Table I. It can be seen that the vibrational coolings were only moderate. The rotational coolings were expected to be much greater, but we could not make a good estimate of their magnitudes.

The calibration of the photoelectron kinetic energy was done with the Ar^+ $^2P_{3/2}$ photoelectron peak, which had a resolution of 13 meV when the analyzer was operated at 1 eV pass energy. Under the high temperature conditions, the kinetic energy scale drifted faster, so we took shorter scans within less than an hour, and then added the spectra to achieve better statistics. The resolution was degraded to the range 15–20 meV in the final spectrum.

III. Method of Theoretical Calculations

The ground states of all the group IV–VI diatomics are $^1\Sigma^+$ states arising from the valence configuration of $1\sigma^2 2\sigma^2 3\sigma^2 1\pi^4$. The 3σ orbital is expected to be a strongly bonding orbital formed from the p_z orbitals of the two atoms along the internuclear axis. The 1π orbital should be a bonding orbital formed from the p_x and p_y orbitals of the two atoms, with the group VI atom contributing more than the group IV atom for the heavier species. For oxides and sulfides, this is a nonbonding or weakly bonding chalcogen orbital.

The ionization of an electron from the 1π orbital should lead to a $^2\Pi$ state described by a $1\sigma^2 2\sigma^2 3\sigma^2 1\pi^3$ configuration. The removal of a 3σ electron would result in a $^2\Sigma^+$ state with a $1\sigma^2 2\sigma^2 3\sigma 1\pi^4$ configuration. Spin–orbit interaction would split the $^2\Pi$ state into two spin-orbit components, $^2\Pi_{1/2}$ and $^2\Pi_{3/2}$. As the relativistic effect becomes stronger for the heavy molecules, it is more appropriate to represent these two states with the Ω quantum numbers, 1/2 and 3/2. The same is true for the $^2\Sigma^+$ state, for which the Ω designation 1/2 would be more appropriate in the relativistic limit. For convenience, however, we will still use the labelings $^2\Pi_{1/2}$, $^2\Pi_{3/2}$, and $^2\Sigma^+$ or $^2\Sigma^+_{1/2}$, or where needed for clarity, we shall use both labelings interchangeably.

It is known from earlier relativistic calculations by one of us (K.B.)[13] that the $^2\Pi$ and $^2\Sigma^+$ states cross for SnO, PbO, and PbS. In the relativistic limit, the $^2\Pi_{1/2}$ and $^2\Sigma^+_{1/2}$ states have the same symmetry and can interact with each other. Consequently, the influence of the spin–orbit coupling and the exact region of avoided crossings for the heavier molecules could be very interesting.

We carried out complete active space MCSCF (CASSCF), followed by multireference singles + doubles CI (MRSDCI) calculations on the low-lying electronic states of $SnSe^+$, $SnTe^+$, $PbSe^+$, and $PbTe^+$, and the ground state of the corresponding neutral species. These calculations were supplemented by relativistic configuration interaction (RCI) calculations of the entire potential energy curves. We used relativistic effective core potentials for all the four atoms described in earlier investigations.[13,15,17,26,27] For the CASSCF and MRSDCI calculations, flexible valence Gaussian basis sets were employed. For Pb and Sn, the outer $d^{10}s^2p^2$ shells were explicitly retained in the MO calculations. The Pb and Sn valence basis sets were of (4*s*4*p*4*d*) quality described in an earlier investigation on PbH_2 and SnH_2.[28] For Se and Te, the outer s^2p^4 shells were explicitly retained in all the calculations. We used comparable (4*s*4*p*) valence + 2 sets of diffuse d-type polarization functions basis resulting in (4*s*4*p*2*d*) basis sets.

In the CASSCF calculations, the orbitals which correlated into the valence s and p orbitals of the individual atoms at infinite separation were included in the active space. These calculations were actually made in the C_{2v} group with the C_2 axis chosen as the intermolecular axis. In this orientation, the active space is composed of four a_1 orbitals, two b_2 orbitals, and two b_1 orbitals. The ten outermost electrons were distributed in all possible ways (full CI) among these orbitals in the CASSCF of the neutral species; the corresponding nine electrons were distributed in all possible ways among these orbitals for the positive ions. Separate CASSCF/CI calculations were carried out for each state of the positive ions and the ground state of the neutral species.

The CASSCF calculations were followed by MRSDCI calculations which included excitations of electrons both into internal and external orbitals. The MRSDCI calculations included all configurations in the CASSCF with coefficients $\geqslant 0.07$ as reference configurations. Subsequently, single and double excitations from all these configurations into all the orbitals were allowed in MRSDCI. The MRSDCI calculations included up to 200 000 configurations.

The spin–orbit effect on the electronic states of these species was addressed through the RCI method. The spin–orbit integrals obtained from relativistic effective core potentials (RECP) were introduced into the CI Hamiltonian matrix. Then all important configurations which mix in the presence of spin–orbit coupling were included in the RCI as reference configurations. For example, the $\Omega = 3/2$ states of the ion included, $^2\Pi_{3/2}(1\sigma^2 2\sigma^2 3\sigma^2 1\pi^3)$, $^2\Pi_{3/2}$ and

$^4\Pi_{3/2}(1\sigma^2 2\sigma^2 3\sigma 4\sigma 1\pi^3)$ and $\Omega = 3/2$ states arising from $1\sigma^2 2\sigma^2 3\sigma^2 1\pi^2 2\pi$ configuration. The final RCI calculations of the 3/2 states included 20 reference configurations. The RCI calculations for the 1/2 states included $^2\Pi_{1/2}(1\sigma^2 2\sigma^2 3\sigma^2 1\pi^3)$, $^2\Sigma^+_{1/2}(1\sigma^2 2\sigma^2 3\sigma 1\pi^4, 1\sigma^2 2\sigma^2 3\sigma 4\sigma 1\pi^3)$ and 1/2 states arising from $1\sigma^2 2\sigma^2 3\sigma^2 1\pi^2 2\pi$ configuration. The RCI calculations were done for the entire potential energy curves of the neutral and ionic species.

All the CASSCF/MRSDCI calculations were done using a modified version by one of us (K.B.)[29] of ALCHEMY II codes[30] to include RECPs. The RCI calculations were done using the method described in Ref. 28.

IV. RESULTS AND DATA ANALYSIS

The photoelectron spectra of $SnSe^+$, $SnTe^+$, $PbSe^+$, and $PbTe^+$ are shown in Figs. 3–6, respectively. The four spectra look very similar except that the spin–orbit splitting in the Π bands increases from $SnSe^+$ to $PbTe^+$. The $^2\Sigma^+$ bands, arising from removal of electrons from the 3σ orbitals, are very sharp, with relatively little vibrational excitation. This implies that the 3σ orbital is a nonbonding or weak bonding orbital, just opposite to what we would have expected. The $^2\Pi$ bands are split into two spin–orbit bands $^2\Pi_{1/2}$ and $^2\Pi_{3/2}$ with very rich vibrational excitation, indicating that the π orbital is a rather stongly bonding orbital. The two bands overlap heavily in $SnSe^+$, and become well separated in $PbTe^+$ as the spin–orbit effect gets stronger. It is interesting to note that the spin–orbit splitting is larger in $SnTe^+$ than that in $PbSe^+$, indicating that the group VI atom contributes more to the π orbital than the group IV atom does.

No other photoelectron bands were observed at higher binding energy than that of $^2\Sigma^+$ in all cases. The 1σ orbitals presumably have too high energies to be accessed by the HeI (584 Å) radiation. At the HeI energy, the 2σ orbitals have too low ionization cross sections to be observed under our experimental conditions.[7] However, we observed two extra bands marked as "AI" in the $PbTe^+$ spectra at low energy. These two bands or shoulders, resembling the two Π bands, do not arise from impurities, and were not affected by changing from Ne to He carrier gas. Based on the resemblance of these two bands to the main Π bands, we assign them as autoionization transitions, as it is well known that autoionization can markedly alter the Franck–Condon factors from those of the direct ionization processes.[31] This would imply that there must be a resonant absorption at about 584 Å for PbTe, which has not been observed to our knowledge.

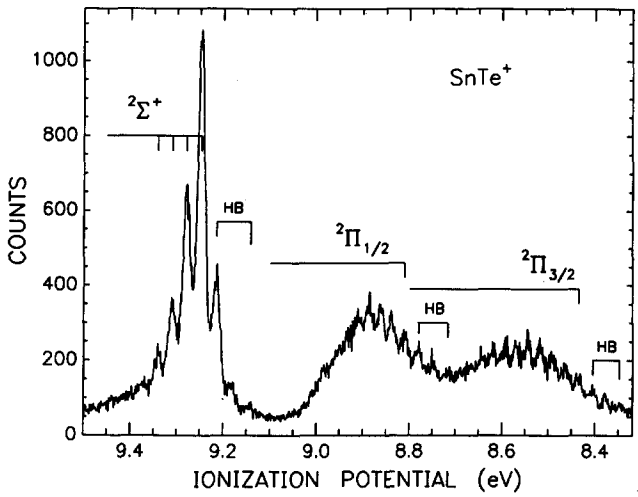

FIG. 4. The HeI photoelectron spectrum of $SnTe^+$. HB means hot band transitions.

Vibrational structure was well resolved for all the spectra except $PbTe^+$, which has very low vibrational frequencies. There are pronounced hot band transitions in $SnTe^+$ and $PbSe^+$, labeled as "HB" in the figures. The ionization potentials (IPs) and vibrational frequencies were easily obtained for the $^2\Sigma^+$ states from the sharp spectra. For the Π bands, the vertical IPs were obtained by fitting a Gaussian to each band, and the mean values of the Gaussians were taken as the vertical IPs. Two factors complicate extraction of the adiabatic IPs: the hot band transitions and the overlapping nature of the two Π bands. The observation of autoionizations in $PbTe^+$ indicates that the ground vibrational levels in

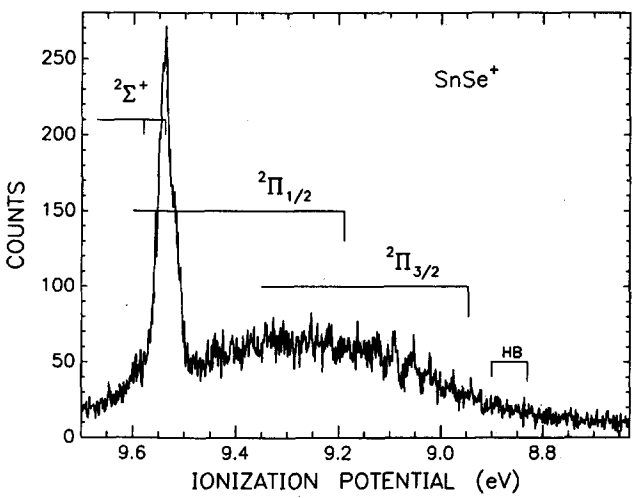

FIG. 3. The HeI photoelectron spectrum of $SnSe^+$. HB means hot band transitions.

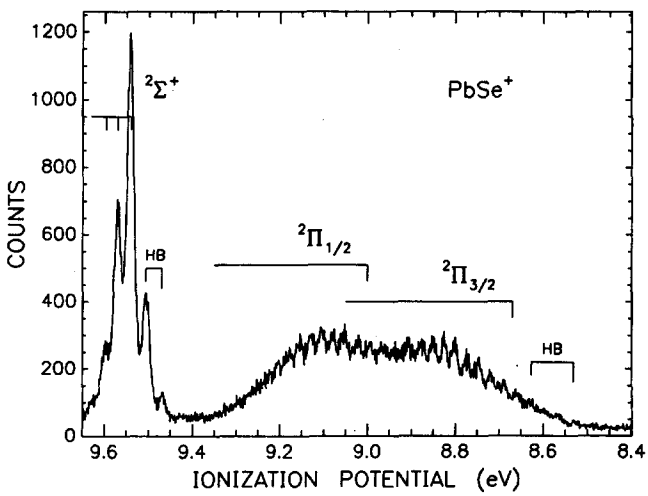

FIG. 5. The HeI photoelectron spectrum of $PbSe^+$. HB means hot band transitions.

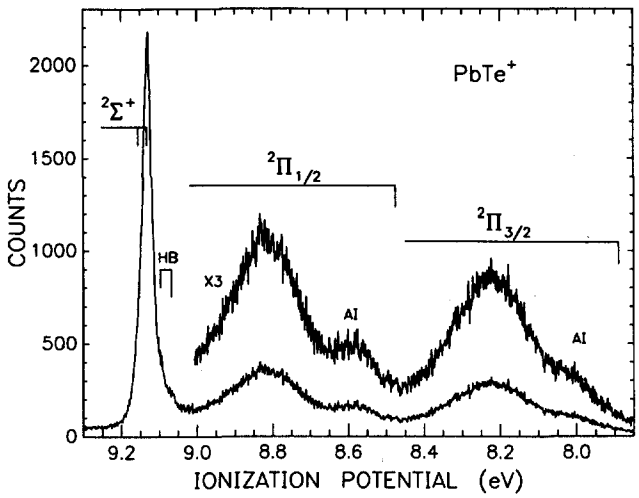

FIG. 6. The HeI photoelectron spectrum of $PbTe^+$. HB means hot band transitions. The shoulders marked as "AI" are assigned to autoionization.

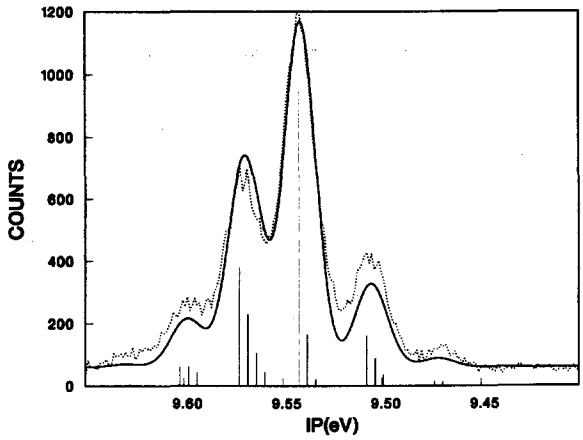

FIG. 7. A Franck–Condon factor calculation for the $^2\Sigma_{1/2}^+$ band of $PbSe^+$. The dotted curve is the experimental spectrum. The lines are the individual Franck–Condon factors. The solid curve is the spectrum calculated by convoluting each line with a Gaussian (0.018 eV width).

the Π bands may not be reached by vertical transitions. Therefore, the experimentally derived adiabatic IPs may be taken only as upper bounds.

In order to obtain the equilibrium bond lengths for the individual ionic states, we have performed Franck–Condon factor calculations. In addition to the equilibrium bond length, a Franck–Condon factor analysis also can yield the vibrational temperature and a refined value of the vibrational frequency. It can also help estimate the adiabatic ionization potential.

The Franck–Condon factor calculation adopted here is similar to that used in Ref. 32. It employs a Morse oscillator, described by expansion as a power series in $(r\text{-}r_e)$, where r_e is the equilibrium bond length. The $(r\text{-}r_e)^3$ and $(r\text{-}r_e)^4$ terms were taken as perturbation corrections to the harmonic oscillator Hamiltonian. During the analysis, r_e and Tvib (the vibrational temperature) were varied systematically until the calculated spectrum was best fitted to the experimental spectrum. For a well-resolved spectrum, r_e was sensitive to within $\pm$ 0.005 Å, Tvib $\pm$ 50 K. In the current analyses, we first calculated the $^2\Sigma^+$ bands because they have sharp structure and easily recognizable hot bands. A fit for the $^2\Sigma^+$ band of $PbSe^+$ is shown in Fig. 7, from which we obtained $r_e = 2.547$ Å, and Tvib = 500 K. We then used the Tvib to fit the Π bands, for which we adjusted the r_e and the adiabatic IP to get the best fit. Figure 8 shows such a fit for the $^2\Pi_{3/2}$ band of $PbSe^+$. It can be seen from Fig. 7 and Fig. 8 that the hot bands can make the spectrum very complicated. The experimental spectrum is really a superposition of the transitions from the ground vibrational state and all the hot band transitions. This could be more serious without the supersonic cooling.

It should be pointed out that the Franck–Condon factor calculation is only approximate. It tends to underestimate the Franck–Condon factors for high vibrational levels in the final states. For the Π bands of $PbTe^+$, too many vibrational levels were needed, and the calculation was no longer feasible. It may also be that the final-state potential energy curves are too shallow for a Morse oscillator representation to be adequate.

All the derived IPs and spectroscopic constants are tabulated in Tables II–V for $SnSe^+$, $SnTe^+$, $PbSe^+$, and $PbTe^+$, respectively, along with the theoretical values. The experimental vibrational frequencies for the Π bands of $PbTe^+$ are only estimates. The Tvibs have been given in Table I.

V. DISCUSSION

A. Comparisons between experimental and theoretical spectroscopic constants

The theoretical potential energy curves near the minima were fitted to a cubic polynomial to obtain the theoretical r_e and ω_e values of the various states. Figs. 9–12 show the RCI potential energy curves of the (SnSe, $SnSe^+$), (SnTe, $SnTe^+$), (PbSe, $PbSe^+$), and (PbTe, $PbTe^+$) pairs, respectively. Tables II–V show the experimental and theoretical spectroscopic constants of the ground neutral and ionic states of the four molecules. The experimental spectroscopic

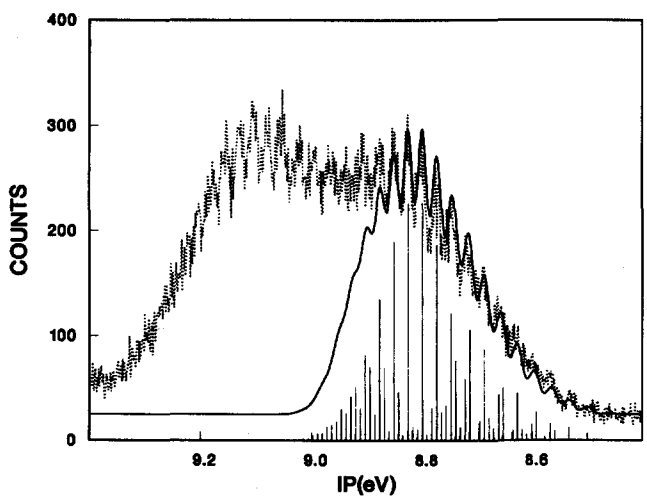

FIG. 8. A Franck–Condon factor calculation for the $^2\Pi_{3/2}$ band of $PbSe^+$. The dotted curve is the experimental spectrum. The lines are the individual Franck–Condon factors. The solid curve is the spectrum calculated by convoluting each line with a Gaussian (0.020 eV width).

TABLE II. Spectroscopic constants of SnSe[a] and $SnSe^+$.

		r_e (Å)		ω_e (cm^{-1})		IP_{ad} (eV)		IP_{vt} (eV)		D_e (eV)	
		Theo.	Expt.	Theo.	Expt.	Theo.	Expt.	Theo.	Expt.	Theo.	Expt.
SnSe	$^1\Sigma^+$	2.38	2.3256	324	331.2					4.23	4.20
$SnSe^+$	$^2\Pi_{3/2}$	2.55	2.48(1)	257	300(10)	9.20	8.947(10)	9.30	9.092(10)	2.26	2.60
	$^2\Pi_{1/2}$	2.56	2.48(1)	259	300(10)	9.44	9.189(10)	9.53	9.323(10)	2.02	2.35
	$^2\Sigma^+_{1/2}$	2.38	2.34(1)	(274)	310(15)	9.85	9.540(7)				

[a]The experimental spectroscopic constants for the neutral $^1\Sigma^+$ ground state are from Ref. 33.

TABLE III. Spectroscopic constants of SnTe[a] and $SnTe^+$.

		r_e (Å)		ω_e (cm^{-1})		IP_{ad} (eV)		IP_{vt} (eV)		D_e (eV)	
		Theo.	Expt.	Theo.	Expt.	Theo.	Expt.	Theo.	Expt.	Theo.	Expt.
SnTe	$^1\Sigma^+$	2.59	2.5228	243	259.5					3.30	3.69
$SnTe^+$	$^2\Pi_{3/2}$	2.75	2.668(5)	203	210(6)	7.93	8.435(7)	8.14	8.545(7)	2.10	2.59
	$^2\Pi_{1/2}$	2.76	2.643(5)	205	200(6)	8.33	8.814(7)	8.40	8.864(7)	1.75	2.22
	$^2\Sigma^+_{1/2}$	2.58	2.566(5)	234	255(5)	8.76	9.247(7)				

[a]The experimental spectroscopic constants for the neutral $^1\Sigma^+$ ground state are from Ref. 33.

TABLE IV. Spectroscopic constants of PbSe[a] and $PbSe^+$.

		r_e (Å)		ω_e (cm^{-1})		IP_{ad} (eV)		IP_{vt} (eV)		D_e (eV)	
		Theo.	Expt.	Theo.	Expt.	Theo.	Expt.	Theo.	Expt.	Theo.	Expt.
PbSe	$^1\Sigma^+$	2.45	2.4022	268	277.6					3.5	3.1
$PbSe^+$	$^2\Pi_{3/2}$	2.66	2.577(5)	207	210(6)	8.72	8.671(1)	8.82	8.800(7)	1.38	1.82
	$^2\Pi_{1/2}$	2.67	2.547(5)	205	210(6)	9.04	9.001(7)	9.14	9.104(7)	1.07	1.49
	$^2\Sigma^+_{1/2}$	2.53	2.445(5)	222	242(5)	9.64	9.543(7)				

[a]The experimental spectroscopic constants for the neutral $^1\Sigma^+$ ground state are from Ref. 33.

TABLE V. Spectroscopic constants of PbTe[a] and $PbTe^+$.

		r_e (Å)		ω_e (cm^{-1})		IP_{ad} (eV)		IP_{vt} (eV)		D_e (eV)	
		Theo.	Expt.	Theo.	Expt.	Theo.	Expt.	Theo.	Expt.	Theo.	Expt.
PbTe	$^1\Sigma^+$	2.67	2.5950	207	212.2					2.76	2.55
$PbTe^+$	$^2\Pi_{3/2}$	2.85		160	(160)	8.50	7.90(4)	8.70	8.22(1)	1.41	2.06
	$^2\Pi_{1/2}$	2.86		160	(160)	9.06	8.48(3)	9.23	8.82(1)	0.85	1.48
	$^2\Sigma^+_{1/2}$	2.76	2.627(5)	(180)	185(8)	9.43	9.131(7)				

[a]The experimental spectroscopic constants for the neutral $^1\Sigma^+$ ground state are from Ref. 33.

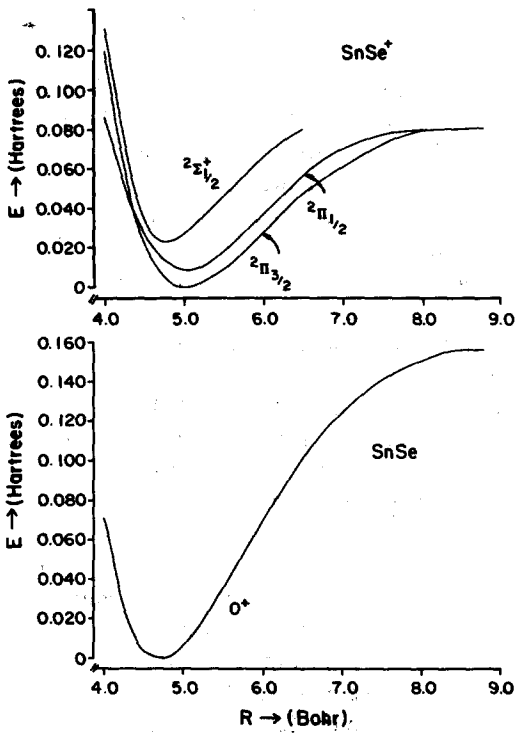

FIG. 9. RCI potential energy curves for SnSe and $SnSe^+$

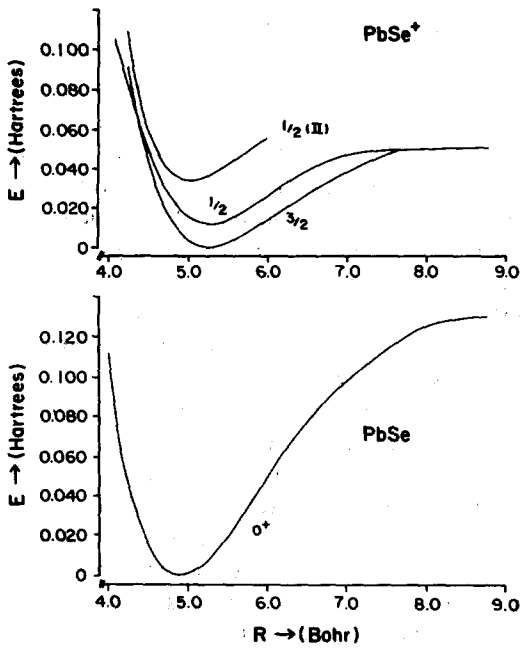

FIG. 11. RCI potential energy curves for PbSe and $PbSe^+$.

constants of the neutral ground states $^1\Sigma^+$ (0^+) are from Ref. 33.

Tables II–V show the theoretical r_e values of the neutral species to be 0.04–0.08 Å longer than the experimental values, the worst case being PbTe. This is anticipated for the level of theory employed here which used relativistic ECPs in conjunction with valence-plus-polarization Gaussian basis sets. The ω_e values are within 2.4%–6.5% of the experimental values for the ground states of the four species. The dissociation energies of the ground states of the neutral species are within 0.7%–10% of the experimental values. The best agreement in the D_es is obtained in SnSe for which the spin–orbit effect is negligible (0.03 eV).

The r_e values of the ionic species are also in very good agreement (3%–6%) with the experimental values. Note that the bond length of the $^2\Sigma^+_{1/2}$ states for all four ions are

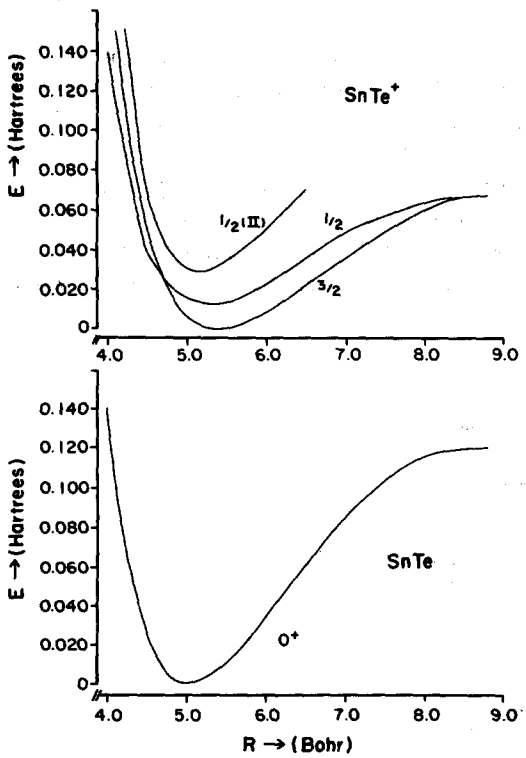

FIG. 10. RCI potential energy curves for SnTe and $SnTe^+$.

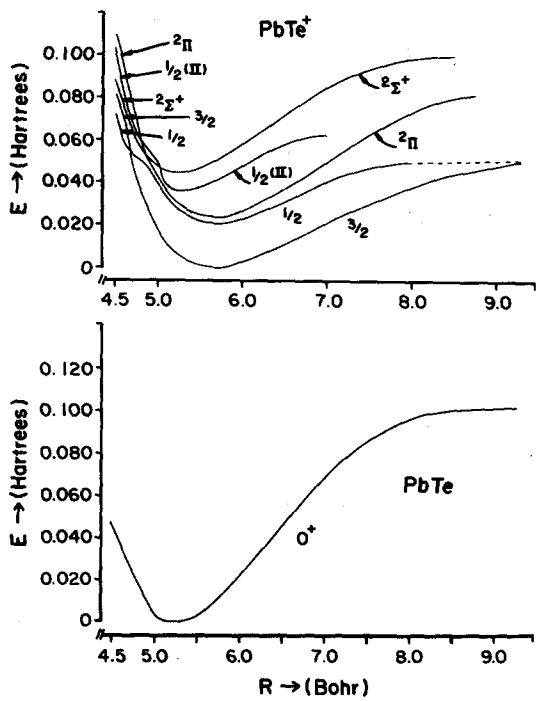

FIG. 12. RCI potential energy curves for PbTe and $PbTe^+$. The curves labeled as $^2\Sigma^+$ and $^2\Pi$ are simple HF calculations without taking into account the relativistic effect.

shorter in comparison to those of the $^2\Pi_{1/2}$ and $^2\Pi_{3/2}$ states and similar to those of the ground $^1\Sigma^+$ states, in agreement with the experimental observation that there is very little vibrational excitation in the $^2\Sigma^+_{1/2}$ bands.

The theoretical IPs are within 0.6%–6% of the experimental values. Considering that our basis sets and electron correlation inclusions were just adequate to calculate the IPs of such species, this agreement is very gratifying. For the $^2\Sigma^+_{1/2}$ states, the adiabatic IPs (IP_{ad}s) coincide with the vertical IPs (IP_{vt}s), because the equilibrium bond lengths in the $^2\Sigma^+_{1/2}$ states do not differ much from the neutral ground states ($^1\Sigma^+$), as seen above.

Although the absolute theoretical and experimental energy separations of the $^1\Sigma^+$ state of the neutral species and $^2\Pi_{3/2}$ state of the ions are not in exact agreement, the theoretical and experimental energy separations of the $^2\Pi_{1/2}$ and $^2\Sigma^+_{1/2}$ of the ions relative to $^2\Pi_{3/2}$ agree very well. The ground state theoretical spin–orbit splitting ($^2\Pi_{3/2}$–$^2\Pi_{1/2}$ separation) of $PbTe^+$ is 4518 cm^{-1} compared to an approximate value of 4680 cm^{-1} obtained from the photoelectron spectrum of PbTe. Similarly, the $^2\Pi_{3/2}$–$^2\Sigma^+_{1/2}$ experimental and theoretical vertical separations are 1.23 and 0.93 eV, respectively.

As seen from Table IV, the agreement between theoretical and experimental IPs for PbSe are in the best agreement among the four species, indicating that both electron correlation effects and spin-orbit effects were included in a consistent way for PbSe. The theoretical spin–orbit splitting for the ground state ($^2\Pi_{3/2}$–$^2\Pi_{1/2}$) is 2585 cm^{-1} compared to the present experimental value of 2660 cm^{-1}.

The experimental D_es of the ionic states were calculated using the formula:

$$D_e(MCh^+) = IP(M) - IP(MCh) + D_e(MCh),$$

where IP(M) is the ionization potential of the group IV atom taken from Ref. 34, IP(MCh) is the ionization potential of the group IV–VI diatomics and D_e(MCh) is the experimental dissociation energy of the neutral $^1\Sigma^+$ ground state of the chalcogenide. The theoretical D_es of MCh^+ were obtained from the RCI calculations at r_e and long distance. Consequently, the theoretical values include the spin–orbit coupling effect more accurately than the electron correlation effects.

B. Nature of the electronic states and the potential energy curves

The ground states of all four species are described predominantly by the $1\sigma^2 2\sigma^2 3\sigma^2 1\pi^4$ configuration near the equilibrium geometries. As mentioned before, the ionization of a π electron leads to the spin–orbit split $^2\Pi_{1/2,3/2}$ states arising from the $1\sigma^2 2\sigma^2 3\sigma^2 1\pi^3$ configuration. The removal of a 3σ electron leads to $^2\Sigma^+_{1/2}$ state.

The relative ordering of the $^2\Sigma^+$ and $^2\Pi$ states depends on the internuclear distance. At short distances, the $^2\Sigma^+$ state is lower in energy while at longer distances the $^2\Pi$ state is lower. In CO^+, which has a very short bond length, the $^2\Sigma^+$ state is indeed lower than the $^2\Pi$ state.[35] This is in contrast to the current situation, where the $^2\Pi$ states are lower than the $^2\Sigma^+$ state, because here the bond lengths are much longer. The $^2\Sigma^+$ and $^2\Pi$ potential energy curves would cross in the absence of the spin–orbit coupling for all four ions. This crossing induces an avoided crossing in the $\Omega = 1/2$ states in the presence of spin–orbit coupling, as shown in Figs. 9–12. The avoided crossing has been found also in PbO^+, PbS^+, and SnO^+,[13] indicating the importance of the relativistic effect in these heavy molecules.

The avoided crossings in the $\Omega = 1/2$ states can be best understood through analyses of the RCI wave functions vs internuclear distances. For example, the lowest 1/2 state denoted by 1/2(I) of $PbTe^+$ is 82% $^2\Sigma^+_{1/2}$ and 0.4% $^2\Pi_{1/2}$ at 4.75 bohr. However, at 5.00 bohr, it becomes 83% $^2\Pi_{1/2}$ and 0.4% $^2\Sigma^+_{1/2}$. The second root of the $\Omega = 1/2$ RCI calculations denoted by 1/2(II) exhibits approximately the opposite behavior. That is, at short distances, the 1/2(II) state is predominantly $^2\Pi_{1/2}$, but it switches to $^2\Sigma^+_{1/2}$ at 5.0 bohr.

The avoided crossing discussed above results in shoulders in the 1/2 states of $PbTe^+$ and $PbSe^+$. The crossing of the $^2\Pi_{3/2}$ curve with the $^2\Pi_{1/2}$ curve is also due to the above-mentioned avoided crossing.

Photoelectron spectroscopy is sensitive to the final-state potential energy surfaces. It especially probes the global ionic potential energy curves for diatomic molecules. From Figs. 9–12, we can see that the $^2\Sigma^+_{1/2}$ states have equilibrium bond lengths very close to that of the $^1\Sigma^+$ ground states, indicating that a Franck–Condon transition from the ground $^1\Sigma^+$ state will fall close to the minimum of the $^2\Sigma^+_{1/2}$ potential energy curve, with a very narrow Franck–Condon

TABLE VI. Gross and overlap Mulliken populations of SnSe, SnTe, PbSe, and PbTe, and their ions after removing a π electron.[a]

		M	Ch	M(*s*)	M(*p*)	M(*d*)	Ch(*s*)	Ch(*p*)	Ch(*d*)	Overlap
SnSe	$^1\Sigma^+$	3.40	6.60	1.74	1.56	0.10	1.99	4.46	0.15	0.758
$SnSe^+$	$^2\Pi$	2.84	6.16	1.87	0.97	0.00	2.01	4.02	0.13	0.334
SnTe	$^1\Sigma^+$	3.51	6.49	1.77	1.65	0.09	2.01	4.35	0.14	0.567
$SnTe^+$	$^2\Pi$	2.94	6.06	1.71	1.07	0.16	2.02	3.90	0.13	0.210
PbSe	$^1\Sigma^+$	3.47	6.53	1.83	1.56	0.08	1.98	4.43	0.12	0.742
$PbSe^+$	$^2\Pi$	2.82	6.18	1.84	0.91	0.06	2.00	4.06	0.13	0.355
PbTe	$^1\Sigma^+$	3.57	6.43	1.84	1.63	0.10	1.96	4.33	0.14	0.541
$PbTe^+$	$^2\Pi$	2.94	6.07	1.85	1.02	0.06	1.98	3.93	0.12	0.236

[a] M stands for the group IV atom. Ch stands for the group VI atom.

region. This is consistent with the observed photoelectron spectra shown in Figs. 3–6.

However, the equilibrium bond lengths of the $^2\Pi_{3/2}$ and $^2\Pi_{1/2}$ states are significantly longer than that of the $^1\Sigma^+$ ground state, and the Franck–Condon transitions should reach the repulsive sides of the $^2\Pi_{3/2}$ and $^2\Pi_{1/2}$ potential energy curves, resulting in broad photoelectron bands as seen in Figs. 3–6. The band shapes should reflect the curvatures of the upper potential energy surfaces. A shallow curve will result in a narrower Franck–Condon region, hence, a narrower band, and a steep curve would give rise to a broader band.

If we closely examine the $^2\Pi_{3/2}$ and $^2\Pi_{1/2}$ bands in Figs. 3–6, we find that the $^2\Pi_{1/2}$ bands are somewhat narrower than the $^2\Pi_{3/2}$ bands. This is particularly obvious in the cases of $SnTe^+$ and $PbTe^+$ where there is less overlap. This difference in band shapes reflects the avoided curve crossing between the $^2\Sigma^+_{1/2}$ and $^2\Pi_{1/2}$ states, because it is the avoided curve crossing which makes the $^2\Pi_{1/2}$ curves look shallower than the $^2\Pi_{3/2}$ curves. These two curves would otherwise look similar at least on the repulsive sides, and give rise to similar photoelectron bands as observed in light molecules such as CO.[35]

The vibrational frequencies, in principle, should also be different. But the difference is too small to be easily observed. There is, nevertheless, a noticeable difference in the case of $SnTe^+$, as seen in Table III.

C. Nature of the chemical bonds of the heavy group IV–VI diatomics

Table VI shows the Mulliken population analyses of the MRSDCI natural orbitals of both the neutral and ionic chalcogenides. Although Mulliken populations cannot be used in an absolute sense due to their basis set dependence, they provide important insight into the nature of bonding in a relative sense. As seen from Table VI, all the neutral chalcogenides in the $^1\Sigma^+$ ground states are quite ionic with the polarity of M^+Ch^-. For example, 0.43 negative charge moves from Pb to Te in the $^1\Sigma^+$ state of PbTe. This charge transfer is even larger for PbSe (0.53 electron), as expected.

As seen from Table VI, $PbTe^+$ in the $^2\Pi$ ground state loses the Pb^+Te^- ionic polarity of the bond, in that the gross population of Te is close to six (6.07). The bonding in $PbTe^+$ is thus considerably less ionic in comparison to PbTe. For $SnTe^+$, also only 0.06 excess charge was found on Te.

For selenides, about 0.16–0.18 excess electron populations are found on Se in the ions. Again, the selenides are similar to the tellurides in that neutral species exhibit greater polarity of bonds.

Comparing the Sn and Pb chalcogenides, we notice that Sn has more charge transfer than Pb, which is opposite to the periodic trend. This is an illustration of the relativistic effect in Pb. The spin–orbit effect and the relativistic inert pair effect in Pb is so strong that the Pb atomic ground state configuration can be approximately described as $(\text{core})6s^2(6p_{1/2})^2(6p_{3/2})^0$. Actually, Pb in its ground state is composed of 88% $^3P_0$ and 12% $^1S_0$.[36] Both the inert-pair effect and the spin–orbit effect result in less charge transfer in the case of Pb compared to Sn.

Another way of viewing the differences in the gross populations of the two atoms in neutral and ionic species is that removal of an electron in the neutral chalcogenides does not take place from the metal atom alone. For example, in the case of PbTe, 63% of the removed electron is from Pb, while the remaining 37% is from Te. Similarly, for PbSe, 65% of the removed electron is from Pb, while 35% is from Se. Note that this trend in the population is consistent with the lower ionization potential of Te compared to Se.

For SnTe, 57% of the removed electron comes from Sn, while 43% comes from Te. For SnSe, 56% of the removed electron comes from Sn, while 44% is from Se. Thus, for SnTe and SnSe, the ionization of a π electron is divided almost equally between the two atoms, while, for PbSe and PbTe, the lead atom sheds a greater percentage of the electron charge.

The individual gross s and p populations of the two atoms are also of interest. The valence populations of the Pb atom are $s^{1.84}p^{1.63}d^{0.10}$ in the ground state of PbTe. For the ion, the corresponding distribution is $s^{1.84}p^{1.02}d^{0.06}$. This implies that most of the 63% of the removed electron is from the Pb $6p$ orbital. The $6s$ population remains the same for both PbTe and PbSe. This is consistent with the relativistic inert pair effect of the Pb $6s$ shell, which is stabilized considerably by the relativistic mass-velocity contraction resulting in extra stability of this shell. This is realized by comparing the s populations of Pb and Sn in different species. The lead atom has a 0.07 larger s population than that of the tin atom.

The valence population of Te in PbTe is $s^{1.96}p^{4.33}$. The extra 0.33 negative charge in the p orbital is due to the polarity of the Pb^+Te^- bond. Again, all of the ionization comes from the p orbitals of Te and Se atoms.

The overlap populations decrease in ionizing the chalcogenides. This suggests weakening of the bonding consistent with smaller $D_e s$ of the ionic species compared to the neutral species. The overlap populations in general decrease as the species become heavier. This trend is also consistent with the smaller $D_e s$ of the heavier chalcogenides.

The photoelectron spectra shown in Figs. 3–6 indicate little vibrational excitation when removing an electron from the 3σ orbital. The bond length of the $^2\Sigma^+_{1/2}$ state does not differ very much from that of the $^1\Sigma^+$ ground state. These results imply that the 3σ orbital is more localized on one atom. Since the bonding is quite ionic in these molecules, this suggests M^+Ch^- character and thus the 3σ orbital should be more localized on the chalcogenide atom. This is in agreement with our theoretical calculations although orbital relaxation effects are found to be significant. Therefore, the chemical bonds in the heavy group IV–VI diatomics can be characterized by being partially ionic and partially covalent through the overlaps of the p orbitals on the two atoms.

VI. CONCLUSIONS

We have measured the photoelectron spectra of $SnSe^+$, $SnTe^+$, $PbSe^+$, and $PbTe^+$ with our new high temperature molecular beam source. Vibrational structure was resolved for all the spectra except for $PbTe^+$. Ionization potentials

and spectroscopic constants were obtained for all the related ionic states. Franck–Condon factor calculations were shown to be very useful in the data analyses. In the $PbTe^+$ spectrum, autoionization transitions were observed.

The relativistic effect was shown to be very important for the heavier molecules. We performed relativistic quantum chemistry calculations to assist the interpretation of the observed photoelectron spectra. The theoretical ionization potentials and spectroscopic constants were in good agreement with the experimental values. In particular, we calculated the relativistic CI potential energy curves for all the involved states, and found that the $\Omega = 1/2$ states ($^2\Pi_{1/2}$ and $^2\Sigma^+_{1/2}$) all underwent avoided curve crossings. The interaction is so strong in $PbTe^+$ that shoulders were developed on the potential energy curves in the avoided crossing region. Experimental evidence for the avoided curve crossings was observed. We further calculated gross and overlap Mulliken populations for all the neutral ground states and the ionic Π states. It was found that appreciable charge transfer occurs from the group IV atoms to the group VI atoms in the neutral ground states. The chemical bond is partially ionic and partially covalent through overlap of the *p* orbitals on the two atoms.

ACKNOWLEDGMENTS

L. S. W. wishes to thank Professor K. S. Pitzer for a valuable discussion and Dr. D. M. Neumark for a copy of the FCF program. K. B. would like to acknowledge the National Science Foundation for Grant No. CHE8818869. This work was supported by the Director, Office of Energy Research, Office of Basic Energy Sciences, Chemical Sciences Division of the U.S. Department of Energy under Contract No. DE-AC03-76SF00098.

[1]See, for example, C. Kittle, *Introduction to Solid State Physics*, 6th ed. (Wiley, New York, 1986).
[2]T. P. Martin, J. Chem. Phys. **77**, 3815 (1982).
[3]L. Brus, J. Phys. Chem. **90**, 2555 (1986).
[4]See, for example, P. Pyykko, Chem. Rev. **88**, 563 (1988); K. Balasubramanian, J. Phys. Chem. **93**, 6585 (1989).
[5]See, for example, J. W. Rabalais, *Principles of Ultraviolet Photoelectron Spectroscopy* (Wiley, New York, 1977).
[6]M. Wu and T. P. Fehlner, J. Am. Chem. Soc. **98**, 7578 (1976).
[7]M. G. White, R. A. Rosenberg, S.-T. Lee, and D. A. Shirley, J. Electron Spectrosc. Relat. Phenom. **17**, 323 (1979).
[8]E. A. Colbourn, J. M. Dyke, A. Fackerell, A. Morris, and I. R. Trickle, J. Chem. Soc. Faraday 2 **73**, 2278 (1977).
[9]E. A. Colbourn, J. M. Dyke, E. P. F. Lee, A. Morris, and I. R. Trickle, Mol. Phys. **35**, 873 (1978).
[10]J. M. Dyke, A. Morris, A. M. A. Ridha, and J. G. Snijders, Chem. Phys. **67**, 245 (1982).
[11]C. Y. Yang and S. Rabii, J. Chem. Phys. **69**, 2497 (1978).
[12]Y. S. Lee, W. C. Ermler, and K. S. Pitzer, J. Chem. Phys. **73**, 360 (1980).
[13]K. Balasubramanian, J. Phys. Chem. **88**, 5759 (1984).
[14]K. Balasubramanian and K. S. Pitzer, Chem. Phys. Lett. **100**, 273 (1983).
[15]K. Balasubramanian, Chem. Phys. Lett. **139**, 262 (1987).
[16]K. Balasubramanian and K. S. Pitzer, J. Phys. Chem. **88**, 1146 (1984).
[17]K. Balasubramanian, J. Chem. Phys. **85**, 1443 (1986).
[18]K. Balasubramanian, Chem. Rev. (in press).
[19]J. E. Pollard, D. J. Trevor, Y. T. Lee, and D. A. Shirley, Rev. Sci. Instrum. **52**, 1837 (1981).
[20]J. E. Reutt, Ph.D. thesis, University of California, Berkeley, 1986, LBL-21322.
[21]L. S. Wang, J. E. Reutt-Robey, B. Niu, Y. T. Lee, and D. A. Shirley, J. Electron Spectrosc. Relat. Phenom. (in press).
[22]R. Colin and J. Drowart, Trans. Faraday Soc. **60**, 673 (1964).
[23]R. F. Porter, J. Chem. Phys. **34**, 583 (1961).
[24]D. A. Northrop, J. Phys. Chem. **75**, 118 (1971).
[25]L.-S. Wang, B. Niu, Y. T. Lee, and D. A. Shirley, Chem. Phys. Lett. **158**, 297 (1989).
[26]K. Balasubramanian, J. Phys. Chem. **91**, 5166 (1987).
[27]K. Balasubramanian and Ch. Ravimohan, J. Mol. Spectrosc. **126**, 220 (1987).
[28]K. Balasubramanian, J. Chem. Phys. **89**, 5731 (1988).
[29]K. Balasubramanian, Chem. Phys. Lett. **127**, 585 (1986).
[30]The major authors of the ALCHEMY II are B. Liu, B. Lengsfield, and M. Yoshiminie.
[31]See, for example, J. H. D. Eland, *Photoelectron Spectroscopy*, 2nd ed. (Butterworth, London, 1984), p. 78.
[32]A. E. Stevens, C. S. Feigerle, and W. C. Lineberger, J. Chem. Phys. **78**, 5420 (1983).
[33]K. P. Huber and G. Herzberg, *Spectroscopic Constants of Diatomics* (Van Nostrand Reinhold, New York, 1979).
[34]C. E. Moore, *Tables of Atomic Energy Levels* (U.S. National Bureau of Standards, Washington, D.C., 1971).
[35]B. Wannberg, D. Nordfors, K. L. Tan, L. Karlsson, and L. Mattsson, J. Electron Spectrosc. Relat. Phenom. **47**, 147 (1988).
[36]K. Balasubramanian and K. S. Pitzer, J. Chem. Phys. **78**, 321 (1983).